Research Article | Vol. 29, No. 11 / 24 May 2021 / Optics Express 16477
Optics EXPRESS

Efficient terahertz generation scheme in a thin-film lithium niobate-silicon hybrid platform

JINGWEI YANG[1] AND CHENG WANG[1,2,*]

[1] *Department of Electrical Engineering, City University of Hong Kong, Kowloon, Hong Kong, China*
[2] *State Key Laboratory of Terahertz and Millimeter Waves, City University of Hong Kong, Kowloon, Hong Kong, China*
[*] *cwang257@cityu.edu.hk*

Abstract: The terahertz (THz) spectral window is of unique interest for plenty of applications, yet we are still searching for a low-cost, continuous-wave, room-temperature THz source with high generation efficiency. Here, we propose and investigate a hybrid lithium niobate/silicon waveguide scheme to realize such an efficient THz source via difference-frequency generation. The multi-layer structure allows low-loss and strong waveguide confinements at both optical and THz frequencies, as well as a reasonable nonlinear interaction strength between the three associated waves. Our numerical simulation results show continuous-wave THz generation efficiencies as high as 3.5×10^{-4} W^{-1} at 3 THz with high tolerance to device fabrication variations, three orders of magnitude higher than current lithium-niobate-based devices. Further integrating the proposed scheme with an optical racetrack resonator could improve the conversion efficiency to 2.1×10^{-2} W^{-1}. Our proposed THz source could become a compact and cost-effective solution for future spectroscopy, communications and remote sensing systems.

1. Introduction

The terahertz (THz) frequency range, generally defined as 0.3 to 10 THz, has fostered many critical scientific and technological applications in medical imaging [1], chemical identification [2], THz radar [3], and THz time-domain spectroscopy [4]. Despite its undoubted usefulness, the THz interval is still relatively unexploited as an "unwrought land" due to the lack of efficient and low-cost THz sources. Researchers have proposed many techniques for THz wave generation using electronic and optical methods [5], including quantum cascaded laser (QCL) [6,7], photoconductive antenna (PCA) [8–10], multiplier chains [11] and difference-frequency generation (DFG) [12–24]. THz-QCLs are capable of providing milliwatt-level THz powers through a cascade of intra-sub-band transitions, but usually require operation at cryogenic temperatures to avoid thermal effects [6], or a relative complex system with integration of a gas cell [7]. PCA-based THz sources have achieved significant conversion efficiencies using plasmonic antenna structures, but the conversion efficiencies of PCA roll off substantially beyond 1 THz, limited by the carrier lifetimes of the semiconductor used [8–10]. Multiplier chains based on Schottky diodes generate THz emission by multiplying the frequency of a microwave source many times, which usually leads to decreasing efficiencies and cumulative noises at high frequencies [11]. As a result, the practical feasibility of current THz systems is still limited by the lack of a compact, continuous-wave, room-temperature THz source with high efficiencies.

Among various techniques, DFG is a particularly interesting scheme for generating continuous-wave THz radiation, by mixing two optical signals whose frequencies are separated by the desired THz frequency [inset of Fig. 1(a)] [12–24]. This approach benefits from the wide availability of high-performance and compact optical lasers, potentially enabling relatively high THz radiation powers at room temperature through a portable device platform. DFG-based THz generation also enjoys a quadratic scaling with frequency (efficiency ~ $\omega_{\mathrm{THz}}{}^2$), ideally suited for applications on the higher end of the THz spectrum. Many second-order (χ^2) nonlinear material platforms,

#419965 https://doi.org/10.1364/OE.419965
Journal © 2021 Received 27 Jan 2021; revised 31 Mar 2021; accepted 5 Apr 2021; published 13 May 2021

Optics EXPRESS

including lithium niobate ($LiNbO_3$, LN) [12–16], gallium phosphide (GaP) [18], gallium arsenide (GaAs) [17,21], zinc telluride (ZnTe) [19], gallium selenide (GaSe) [23] and zinc germanium phosphide (ZGP) [24] have been realized for DFG-based THz generation. Among them, LN is of particular interest for THz-DFG and will be our focus material in this paper, due to its large $\chi^{(2)}$ nonlinear coefficient (390 pm/V in the THz region), relatively high optical damage threshold, and ultra-low optical absorption of ~ 0.001 dB/cm in the near-infrared spectral range [25,26].

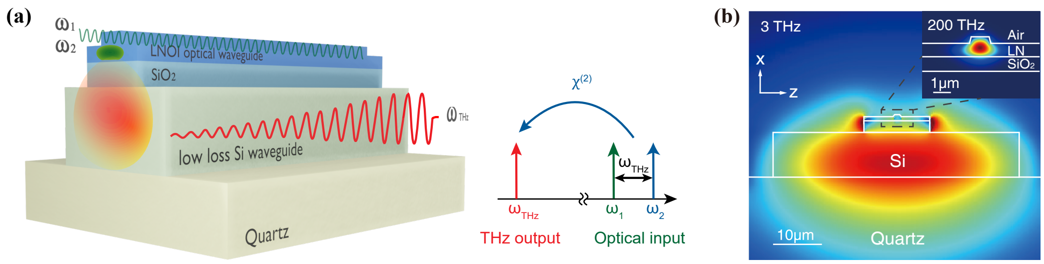

Fig. 1. (a) Schematic diagram of the proposed THz source. Two optical laser signals are injected into the top LNOI optical waveguides, while THz signals are generated and confined in the bottom Si THz waveguide. (b) Numerically simulated electric field distributions (E_z) of the THz mode at 3 THz (main panel) and the optical mode at 200 THz (inset), showing strong field confinement at both frequencies.

Despite the many advantages of LN-based DFG-THz generation, the overall conversion efficiencies have remained relatively low, *i.e.* $< 10^{-7}$ W^{-1} for recently demonstrated waveguide approach [15] and $< 10^{-8}$ W^{-1} in bulk LN crystals (numbers for pulsed operations have been normalized to a continuous-wave scenario) [13,14,16]. Unlike typical nonlinear optical processes where all input and output wavelengths are on the same order, a THz generation process features a large wavelength mismatch between the optical pumps and the created THz wave, often across 2-3 orders of magnitude. As a result, it is particularly challenging to realize strong optical/THz confinement, reasonably high nonlinear interaction strength and phase matching at the same time, compromising the THz conversion efficiency. Another limiting factor is the large THz absorption coefficient of LN, *i.e.* $\alpha = 20$ mm^{-1} at 3 THz [27–29]. The large material absorption limits the maximum DFG interaction lengths in a collinear periodically-poled LN (PPLN) crystal and ultimately the THz generation efficiencies, unless operating at cryogenic temperatures [14,16]. Using a Cherenkov or tilted-pulse-front geometry could greatly alleviate the THz attenuation issue, since the generated THz signal is immediately extracted out of the LN crystal from a different angle with respect to the laser pump [12]. However, the non-collinear configuration also implies that the generated THz signal does not contribute to the coherent nonlinear buildup anymore, leading to a moderate linear power scaling over interaction distance (as opposed to quadratic scaling in a collinear scenario). Most recently, the thin-film LN-on-insulator (LNOI) platform has fostered a number of ultra-efficient nonlinear optical devices, owing to the much stronger light intensity in these sub-wavelength optical structures [30–39]. However, THz generation has not been realized in the LNOI platform, likely due to the large wavelength mismatch between THz and optical waves.

In this paper, we propose a hybrid LNOI/Si coupled-waveguide structure that can dramatically increase the DFG-THz generation efficiencies by satisfying the following requirements simultaneously: strong confinements of both the optical pumps and THz waves, the phase-matching condition, and a long nonlinear interaction distance without significant THz attenuation. The device consists of a top LNOI optical waveguide and a bottom silicon (Si) THz waveguide, as is shown in Fig. 1(a). The ability to independently control the optical and THz device layers allows us to achieve strong confinement and low-loss propagation for both wavelengths, as well as a relatively high nonlinear interaction strength. The theoretically predicted conversion efficiencies are as high as 3.5×10^{-4} W^{-1} at 3 THz with high tolerance to device fabrication variations, three orders of magnitude higher than current LN-based DFG-THz generators. We further show that the conversion efficiencies can exceed 2.1×10^{-2} W^{-1} using an optical resonator structure, without the need of exotic quality (Q) factors or precise alignments of resonance modes.

2. Principle of the THz generator

Figure 1(a) shows the schematic of the proposed device. Two optical laser signals in the telecom band (~ 200 THz, separated by 3 THz) are frequency mixed for generation of 3-THz signal. The top thin-film LN waveguide provides low-loss optical confinement and $\chi^{(2)}$ nonlinearity for the DFG process [31,39]. The bottom THz waveguide co-propagating with the optical waveguide is formed by high-resistivity Si with a low material loss tangent of 10^{-5} at 3 THz [40]. The Si waveguide collects and continuously guides the generated THz waves such that the nonlinear interaction could coherently build up. A 1.5-μm intermediate SiO_2 layer is used to prevent the optical mode from leakage into the Si substrate. Finally, the LN/SiO_2/Si stack sits on top of a quartz substrate with a relatively low THz loss tangent of 10^{-4} at 3 THz [40]. Importantly, the design flexibility in the proposed multi-layer system allows us to independently optimize the effective indices, losses and nonlinear interaction strength of the optical and THz waveguides. Figure 1(b) shows the simulated THz (main panel) and optical (inset) mode profiles, both in transverse-electric (TE) polarization (*i.e.* major electric fields along z-axis of the LN crystal to make use of the d_{33} coefficient), using a finite-difference eigenmode (FDE) solver (Mode Solutions, Anays/Lumerical). Specifically, the top x-cut LN optical waveguide features a width of 1 μm, a rib height of 200 nm and an un-etched slab thickness of 400 nm, allowing for single-mode operation at telecom wavelengths, whereas the bottom Si THz waveguide has a width of ~ 50 μm and a thickness of ~ 8 μm. The optical propagation loss of the LNOI waveguide could be well below 0.1 dB/cm using state-of-the-art LNOI fabrication technologies [31]. The simulated THz loss of the Si waveguide is ~ 7 dB/cm at 3 THz, sufficient to support a total device length of > 1 cm without excessive THz loss, which is crucial for a coherent DFG signal buildup. The simulated loss numbers have taken into account the absorption losses of all materials, including LN [27,28], deposited SiO_2 [41], high-resistivity Si [40] and quartz [40]. Besides loss considerations, we have also optimized the optical-THz nonlinear interaction strength by fine tuning the LN slab thickness, slab width (10 μm, same as the SiO_2 layer width) as well as the Si THz waveguide dimensions, the details of which will be discussed in Section 3.

Despite the need for an unconventional LNOI/Si/quartz substrate, we believe our proposed device configuration can be realized through commercial thin-film production services and standard nanofabrication processes. Silicon-on-quartz substrates are commonly used for THz photonics [42]. For example, Amarloo *et al.* have achieved single-mode THz waveguides using a high-resistivity Si layer of < 100 μm thickness [43]. On the other hand, various choices of substrates for LNOI are already commercially available (*e.g.* NANOLN), including Si, LN, quartz and sapphire, showing the feasibility to achieve strong bonding between the LN thin-film and the Si-on-quartz substrate. Based on the thin-film LN/Si/quartz substrate, the LN optical rib waveguides can first be fabricated using a combination of electron-beam lithography (EBL) and reactive ion etching (RIE) [31]. The Si THz waveguides can subsequently be defined using aligned photolithography followed by standard deep SiO_2/Si dry etching.

To achieve an efficient THz generation process with coherent signal buildup throughout the entire device length, it is important to fulfill the phase-matching condition. In our collinear guided-wave configuration, the phase-matching condition can be expressed as $\Delta k = k_{\mathrm{opt1}} - k_{\mathrm{opt2}}$

Optics EXPRESS

$-\ k_{\mathrm{THz}} = 0$, where $k_{\mathrm{opt1,2}}$ and k_{THz} are the wavevectors of the two pump modes and the THz mode, respectively. Since the two optical frequencies are not too far apart, the wavevector difference k_{opt1} - k_{opt2} can be approximately expressed in terms of the group refractive index $n_{\mathrm{g,opt}}$ (ignoring second- and higher-order dispersion effects). The phase-matching condition is therefore simplified to the matching between optical group index and THz phase index, similar to the velocity matching in an electro-optic modulator:

$$\Delta k = k_{\mathrm{opt1}} - k_{\mathrm{opt2}} - k_{\mathrm{THz}} = \frac{2\pi}{c} f_{\mathrm{THz}} |n_{\mathrm{g,opt}} - n_{\mathrm{THz}}|, \tag{1}$$

In a traditional bulk LN crystal, these wavevectors are usually predetermined by the material refractive indices, requiring a PPLN structure to achieve quasi-phase matching. In contrast, our proposed device configuration allows flexible tuning of the THz effective indices by engineering the Si waveguide dimensions, without the need for periodic domain inversion. Figure 2 shows the numerically simulated effective index (color-coded) at 3 THz as a function of various Si waveguide widths and thicknesses. The dashed line corresponds to a collection of phase-matched structure parameters with an index of $n_{\mathrm{THz}} = 2.27$, which is matched with the optical group index $n_{\mathrm{g,opt}}$ of the LNOI rib waveguide with parameters discussed above. It should be noted that the Si waveguide sees a significant geometric dispersion, *i.e.* n_{THz} changes substantially with frequency. As a result, other waveguide parameters away from the dashed line in Fig. 2 can also support phase-matched THz generation processes, but at shifted THz frequencies (details will be discussed in Section 3). For a fixed waveguide parameter, the phase-matching bandwidth is ~ 25 GHz (full width at half maximum, FWHM) for a device length of 1 cm (inset of Fig. 2), taking into account both geometric and material dispersions.

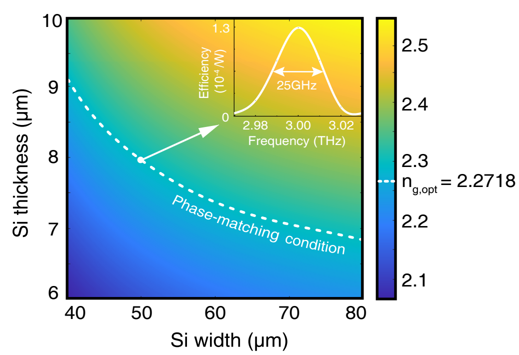

Fig. 2. Phase matching between the THz and optical modes. The 2D color map shows the n_{THz} dependence on the width and thickness of the Si waveguide. The white dashed line corresponds to the structure parameters with $n_{\mathrm{THz}} = 2.27$, which is matched with the optical group index. Inset: THz generation efficiency as a function of THz frequency for a typical Si waveguide with parameters discussed in Section 2, showing a 25-GHz phase-matching bandwidth (FWHM) for a 1-cm device.

3. Theoretical model and device performance

The power evolution of THz waves in our proposed device follows a coupled-mode theoretical model similar to that used in common nonlinear optical waveguides. Here we first consider the case of a lossless waveguide, where the generated DFG signal scales linearly with the optical powers of each pump lasers and quadratically with the device length. The THz generation efficiency Γ (normalized by pump optical power) could be calculated using the following equation [44]:

$$\Gamma = \frac{P_{\text{THz}}}{P_{\text{opt1}} \cdot P_{\text{opt2}}} = \eta L^2 \cdot \text{sinc}^2\left(\frac{\Delta k L}{2}\right), \tag{2}$$

where $P_{\text{opt1,2}}$ are the optical powers of input lasers at ω_1 and ω_2, P_{THz} is the output THz power at ω_{THz}, L is the waveguide length. η is the normalized conversion efficiency (normalized by both pump power and device length) given by:

$$\eta = \frac{2\omega_{\text{THz}}^2 d_{\text{eff}}^2}{n_{\text{opt}}^2 n_{\text{THz}} \varepsilon_0 c^3 A}, \tag{3}$$

where ε_0 and c are the permittivity and speed of light in vacuum, respectively, $\square_{\text{THz}}$ is the angular frequency of the intended THz wave, n_{opt} and n_{THz} are the effective refractive indices of the optical (assuming $n_{\text{opt1}} \approx n_{\text{opt2}}$) and terahertz fundamental TE modes, respectively, and $d_{\text{eff}} = d_{33} = \chi^{(2)}/2 = 195$ pm/V is the effective nonlinear susceptibility at 3 THz, which has taken into account the $\chi^{(2)}$ dispersion due to TO phonon [26], A is the effective spot area between the three waves:

$$A = \frac{A_{\text{opt}}^2 \cdot A_{\text{THz}}}{A_{\text{overlap}}^2} = \frac{\left(\int_{\text{all}} |\mathbf{E}_{\text{opt}}|^2 \text{dxdz}\right)^2 \left(\int_{\text{all}} |\mathbf{E}_{\text{THz}}|^2 \text{dxdz}\right)}{\left|\int_{\text{LN}} |E_{\text{opt,z}}|^2 E_{\text{THz,z}}^* \text{dxdz}\right|^2}, \tag{4}$$

where $\int_{\text{LN}}$ and $\int_{\text{all}}$ denote cross-section integration over the LN region only and all space, respectively. $\mathbf{E}_{\text{opt}}$ and $\mathbf{E}_{\text{THz}}$ are the electric fields of the optical and THz modes and $E_{\text{opt,z}}$ and $E_{\text{THz,z}}$ are their corresponding z components that utilize the largest nonlinear coefficient d_{33}.

When taking into account the absorption of the THz mode [45], the conversion efficiency expression in Eq. (2) can be modified by adding an imaginary part to the phase mismatch as $\Delta k' = \Delta k - i\alpha/2$, where α is the THz attenuation coefficient. The conversion efficiency in lossy medium is then given by:

$$\Gamma' = \eta L^2 \cdot \text{sinc}^2\left(\frac{\Delta k' L}{2}\right) \cdot e^{-\alpha L} = \frac{2\omega_{\text{THz}}^2 d_{\text{eff}}^2}{n_{\text{opt}}^2 n_{\text{THz}} \varepsilon_0 c^3 A} \cdot \text{sinc}^2\left(\frac{(\Delta k - i\alpha/2)L}{2}\right) \cdot L^2 \cdot e^{-\alpha L}, \tag{5}$$

As a result, the overall conversion efficiency shall be optimized not only by minimizing the effective spot area A, but at the same time maintaining a reasonable THz loss. Figure 3(a) shows the dependence of A [as defined in Eq. (4)] and THz loss on the geometry of the Si waveguide. Here the width and thickness of the Si waveguide are changed jointly following the white dashed line in Fig. 2 to ensure the phase-matching condition. While the minimum spot area A takes place at a width of ~ 42 µm, the THz loss shows a continuously decreasing trend with the increase of Si waveguide width. As a result, the optimal structural parameters are dependent on the total device length, since a longer device has more stringent requirement on the THz loss [Fig. 3(b)]. For a 1-cm device, the optimal conversion efficiency of 1.3×10^{-4} W^{-1} in continuous-wave operation can be achieved with a 50-µm width and an 8-µm thickness, the parameters of which have been used for the calculation of THz generation bandwidth in the inset of Fig. 2. For longer devices, the optimal structure shifts towards larger Si waveguide widths to compensate for the increasing cumulative THz losses, as shown in Fig. 3(b). The maximal THz generation efficiencies for 2-cm and 3-cm devices are 2.6×10^{-4} W^{-1} and 3.5×10^{-4} W^{-1} respectively. This indicates that, when the device length is beyond 1 cm, the power scaling characteristic deviates from the quadratic dependence in a lossless model due to significant THz losses [inset of Fig. 3(b)], although the overall conversion efficiency still increases for a longer device. The maximum THz generation achievable in our platform is three orders of magnitude higher than current LN-based DFG

Optics EXPRESS

devices at room temperature [12,15]. Microwatt-level continuous-wave THz emission could be achieved with reasonable optical input powers of ∼ 100 mW and compact device footprint. Such optical power levels are well within the power handling capability of typical LNOI devices, *e.g.* optical powers of ∼ 300 mW in LNOI waveguides and circulation powers of > 50 W in LNOI micro-resonators have been reported [37,38]. Using MgO-doped LNOI thin films could allow even higher input powers, potentially further increasing the achievable THz powers.

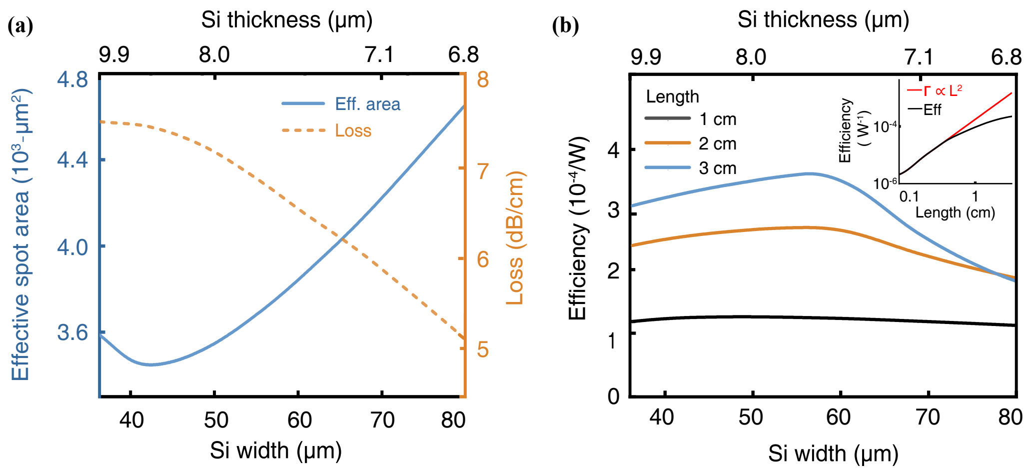

Fig. 3. (a) Effective nonlinear spot area and THz loss versus the THz waveguide dimensions. The waveguide width and thickness are changed jointly following the phase-matching curve in Fig. 2. (b) Conversion efficiency as a function of the THz waveguide dimension in cases of various device lengths. Inset shows the conversion efficiency versus device length in logarithmic scale, showing deviation from ideal quadratical dependence (red line) for device lengths > 1 cm due to THz loss.

Next, we show that the proposed devices feature high tolerance to fabrication variations and alignment inaccuracy. Since the optical group index of the LNOI waveguide (∼ 2.27) is

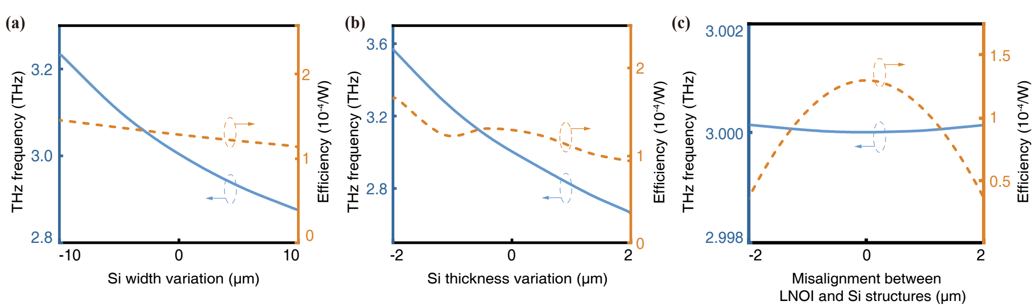

Fig. 4. Tolerance to device fabrication variations. The phase-matched THz output frequency and peak conversion efficiency are plotted as functions of (a) Si width variation, (b) Si thickness variation, and (c) horizontal misalignment between the optical waveguide and Si waveguide.

Optics EXPRESS

relatively insensitive to geometric variations, here we mainly focus on variations in the bottom structures. We first investigate the impact of divergence in Si waveguide width and thickness from a base-case scenario of 50×8 μm, which was previously optimized for 1 cm long device. Interestingly, although deviation in waveguide dimensions moves the THz effective index away from the phase-matching point at 3 THz, a new phase-matching point will emerge at a shifted THz frequency due to the relatively large geometric dispersion. In other words, fabrication variations within a certain range do not lead to performance degradation, but rather tunes the optimal THz generation frequency. For example, as the waveguide width is varied from 40 μm to 60 μm (±10 μm from the base case), the corresponding phase-matched THz frequency would shift from 3.23 to 2.87 THz, while the generation efficiency is only changed by ±11% [Fig. 4(a)]. Similarly, a ±2-μm variation in the waveguide thickness changes the THz frequency over a range of 0.90 THz, with the efficiency varying within ±22% [Fig. 4(b)]. Indeed, this tuning characteristic could provide a simple and effective way to engineer the output THz frequency of the proposed source. Another possible fabrication error is the misalignment between the optical waveguide and the bottom Si waveguide, the effect of which is shown in Fig. 4(c). We find that the output THz frequency and conversion efficiency are not affected much by fabrication misalignment. An alignment error of ±1 μm, which is achievable in most academic mask aligners, leads to a negligible change in the THz frequency and a modest 4.6% drop in the conversion efficiency [Fig. 4(c)].

4. Efficiency improvement using a resonant structure

The THz generation efficiency of our proposed scheme can be further improved by two orders of magnitude using a racetrack optical resonator, as is shown in Fig. 5(a). The multi-layer structural parameters remain the same as in previous designs, such that the phase-matching condition can still be satisfied. Instead of running the optical pumps through the device only once, this resonator configuration can fully exploit the low-loss property of the LNOI platform and dramatically increase the effective pump powers inside the optical cavity. Here we only harness the THz signals generated in one straight section of the racetrack resonator [bottom section in Fig. 5(a)], whereas signals generated from other parts of the resonator will not be collected due to the large wavevector mismatch. We assume a racetrack resonator with a bending radius of 80 μm and a straight-section length of 2 mm, which is critically coupled with a loaded Q factor of 1×10^6. The parameters chosen here are well achievable in the LNOI platform, as ultrahigh resonator Q factors over 10^7 have already been demonstrated [31,39]. In this case, the free-spectral range (FSR) is estimated as 30 GHz (resonator circumference length $L = 4.5$ mm), with a linewidth of 200 MHz, leading to a finesse of 150 and an average round-trip number of ∼ 24 (Finesse/2π). As a result, the effective pump power sees a 48-times amplification inside the resonator compared with the power in the bus waveguide in a critical coupling scenario. If both optical pumps are tuned into resonance, the system conversion efficiency is enhanced by a factor of ~2,280 from a 2-mm waveguide device (9.3×10^{-6} W^{-1}), to 2.1×10^{-2} W^{-1}, representing a two orders of magnitude increase from the non-resonant best-case scenario with a more compact footprint. It should be noted that the choice of racetrack resonator size within a certain range (*e.g.* straight-section length of 1 ∼ 3 mm) does not change the overall THz generation efficiency much, since a smaller resonator leads to higher circulating power but shorter THz accumulation distance. Here we choose a 2-mm length to minimize the impact of THz loss (∼ 1.4 dB) while maintaining a high straight-to-bend length ratio (∼ 80%). Meanwhile, the scattering loss of the generated THz signal at the resonator bending area can be controlled to within 0.5 dB without special design, according to our numerical FDTD simulation result.

A common challenge in resonator-based nonlinear optical systems is the difficulty to precisely match the resonant frequencies of all associated modes within the phase-matching bandwidth. Here we show that our proposed system could readily achieve mode matching and phase matching

Optics EXPRESS

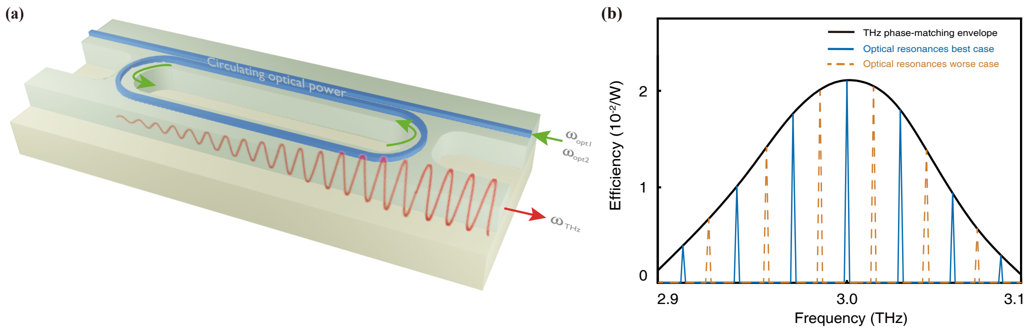

Fig. 5. (a) Schematic illustration of the advanced device architecture with an embedded racetrack resonator to enhance the effective pump power. (b) Phase-matching envelope (black) and the distribution of optical resonance modes (blue solid curve for perfect alignment and orange dashed curve for the worst-case scenario) for a 2-mm racetrack device showing high robustness for mode and phase-matching.

without special engineering and precise frequency alignment. For the 2-mm device discussed above, the phase-matching bandwidth (FWHM) is ~ 100 GHz, while the resonator FSR is 30 GHz. Therefore we can straightforwardly choose two optical resonance modes that are separated by ~ 3 THz, which automatically fall inside the phase-matching bandwidth. The blue solid curve in Fig. 5(b) shows the best-case scenario where the optical resonance frequency difference is exactly matched with the phase-matching peak. Even for the worst case (orange dashed curve), where the phase-matching peak falls right in the middle of two optical resonance modes, the overall conversion efficiency Γ is only compromised by 2.4% from the optimal case, showing high robustness for practical applications. We also note that this feature of straightforward mode/phase-matching is not affected by the resonator size, since a smaller device gives rise to coarser resonances but at the same time a larger phase-matching bandwidth.

5. Conclusions and outlook

In conclusion, we have investigated an efficient continuous-wave THz source based on a hybrid LNOI/silicon platform. The proposed multi-layer structure allows us to independently design the optical and THz waveguides to achieve strong confinement and low loss for both frequencies, yielding an efficient DFG process. Our numerical calculation shows conversion efficiencies as high as 3.5×10^{-4} W^{-1} in a 3-cm waveguide device. Using a racetrack resonator structure, we show the THz generation efficiency can be further increased to 2.1×10^{-2} W^{-1}, orders of magnitude higher than current DFG-based THz sources.

Looking ahead, a frequency switchable continuous-wave THz source could be realized by implementing an array of the proposed waveguides with incremental phase-matching frequencies. Fast switching of the THz frequency can be achieved by electro-optically routing the pump signals into different channels on demand, leveraging the high-performance electro-optic functionality in the LNOI platform. Furthermore, the optical-based THz generator allows straightforward signal modulation at GHz data bandwidths, using either off-chip or on-chip LN electro-optic modulators [30,36], ideally suited for THz communications applications. We envision the proposed continuous-wave THz source to find a wide variety of applications including spectroscopy, communications and remote sensing.

Optics EXPRESS

Funding. National Natural Science Foundation of China (61922092); Research Grants Council, University Grants Committee (CityU 11204820, CityU 21208219); City University of Hong Kong (9610402, 9610455, 9667182).

Acknowledgements. The authors acknowledge valuable discussions with Dr. Xiuquan Zhang from NANOLN about the production feasibility of the proposed LNOI/Si wafer, and Dr. Marc Jankowski on the theoretical model.

Disclosures. The authors declare no conflicts of interest.

Data availability. Data underlying the results presented in this paper are not publicly available at this time but may be obtained from the authors upon reasonable request.

References

1. Z. D. Taylor, R. S. Singh, D. B. Bennett, P. Tewari, C. P. Kealey, N. Bajwa, M. O. Culjat, A. Stojadinovic, H. Lee, and J. P. Hubschman, "THz medical imaging: in vivo hydration sensing," IEEE Trans. Terahertz Sci. Technol. **1**(1), 201–219 (2011)..
2. Y. Shen, T. Lo, P. Taday, B. Cole, W. Tribe, and M. Kemp, "Detection and identification of explosives using terahertz pulsed spectroscopic imaging," Appl. Phys. Lett. **86**(24), 241116 (2005)..
3. K. B. Cooper, R. J. Dengler, N. Llombart, B. Thomas, G. Chattopadhyay, and P. H. Siegel, "THz Imaging Radar for Standoff Personnel Screening," IEEE Trans. Terahertz Sci. Technol. **1**(1), 169–182 (2011)..
4. P. U. Jepsen, D. G. Cooke, and M. Koch, "Terahertz spectroscopy and imaging–Modern techniques and applications," Laser Photonics Rev. **5**(1), 124–166 (2011)..
5. G. K. Kitaeva, "Terahertz generation by means of optical lasers," Laser Phys. Lett. **5**(8), 559–576 (2008)..
6. R. Köhler, A. Tredicucci, F. Beltram, H. E. Beere, E. H. Linfield, A. G. Davies, D. A. Ritchie, R. C. Iotti, and F. Rossi, "Terahertz semiconductor-heterostructure laser," Nature **417**(6885), 156–159 (2002).
7. P. Chevalier, A. Armizhan, F. Wang, M. Piccardo, S. G. Johnson, F. Capasso, and H. O. Everitt, "Widely tunable compact terahertz gas lasers," Science **366**(6467), 856–860 (2019).
8. C. W. Berry, N. Wang, M. R. Hashemi, M. Unlu, and M. Jarrahi, "Significant performance enhancement in photoconductive terahertz optoelectronics by incorporating plasmonic contact electrodes," Nat. Commun. **4**(1), 1622 (2013).
9. S. Nellen, T. Ishibashi, A. Deninger, R. B. Kohlhaas, L. Liebermeister, M. Schell, and B. Globisch, "Experimental Comparison of UTC- and PIN-Photodiodes for Continuous-Wave Terahertz Generation," J. Infrared, Millimeter, Terahertz Waves **41**(4), 343–354 (2020).
10. T. Harter, S. Muehlbrandt, S. Ummethala, A. Schmid, S. Nellen, L. Hahn, W. Freude, and C. Koos, "Silicon-plasmonic integrated circuits for terahertz signal generation and coherent detection," Nat. Photonics **12**(10), 625–633 (2018)..
11. G. Chattopadhyay, E. Schlecht, J. S. Ward, J. J. Gill, H. H. Javadi, F. Maiwald, and I. Mehdi, "An all-solid-state broad-band frequency multiplier chain at 1500 GHz," IEEE Trans. Microwave Theory Tech. **52**(5), 1538–1547 (2004).
12. S. Bodrov, M. Bakunov, and M. Hangyo, "Efficient Cherenkov emission of broadband terahertz radiation from an ultrashort laser pulse in a sandwich structure with nonlinear core," J. Appl. Phys. **104**(9), 093105 (2008)..
13. L. Pálfalvi, J. Fülöp, and J. Hebling, "Absorption-reduced waveguide structure for efficient terahertz generation," Appl. Phys. Lett. **107**(23), 233507 (2015)..
14. S. W. Huang, E. Granados, W. R. Huang, K. H. Hong, L. E. Zapata, and F. X. Kärtner, "High conversion efficiency, high energy terahertz pulses by optical rectification in cryogenically cooled lithium niobate," Opt. Lett. **38**(5), 796–798 (2013).
15. K. Suizu, K. Koketsu, T. Shibuya, T. Tsutsui, T. Akiba, and K. Kawase, "Extremely frequency-widened terahertz wave generation using Cherenkov-type radiation," Opt. Express **17**(8), 6676–6681 (2009).
16. S. Carbajo, J. Schulte, X. Wu, K. Ravi, D. N. Schimpf, and F. X. Kärtner, "Efficient narrowband terahertz generation in cryogenically cooled periodically poled lithium niobate," Opt. Lett. **40**(24), 5762–5765 (2015).
17. M. Nagai, K. Tanaka, H. Ohtake, T. Bessho, T. Sugiura, T. Hirosumi, and M. Yoshida, "Generation and detection of terahertz radiation by electro-optical process in GaAs using 1.56 µm fiber laser pulses," Appl. Phys. Lett. **85**(18), 3974–3976 (2004)..
18. J. Hebling, G. Almási, I. Z. Kozma, and J. Kuhl, "Velocity matching by pulse front tilting for large-area THz-pulse generation," Opt. Express **10**(21), 1161–1166 (2002).
19. T. Löffler, T. Hahn, M. Thomson, F. Jacob, and H. Roskos, "Large-area electro-optic ZnTe terahertz emitters," Opt. Express **13**(14), 5353–5362 (2005).
20. W. Shi and Y. J. Ding, "Designs of terahertz waveguides for efficient parametric terahertz generation," Appl. Phys. Lett. **82**(25), 4435–4437 (2003)..
21. A. Marandi, T. E. Darcie, and P. P. M. So, "Design of a continuous-wave tunable terahertz source using waveguide-phase-matched GaAs," Opt. Express **16**(14), 10427–10433 (2008).
22. K. Saito, T. Tanabe, Y. Oyama, K. Suto, and J. Nishizawa, "Terahertz-wave generation by GaP rib waveguides via collinear phase-matched difference-frequency mixing of near-infrared lasers," J. Appl. Phys. **105**(6), 063102 (2009)..
23. Y. J. Ding, "High-Power Tunable Terahertz Sources Based on Parametric Processes and Applications," IEEE J. Sel. Top. Quantum Electron. **13**(3), 705–720 (2007)..

Optics EXPRESS

24. D. Creeden, J. C. McCarthy, P. A. Ketteridge, P. G. Schunemann, T. Southward, J. J. Komiak, and E. P. Chicklis, "Compact, high average power, fiber-pumped terahertz source for active real-time imaging of concealed objects," Opt. Express **15**(10), 6478–6483 (2007)..
25. D. N. Nikogosyan, *Nonlinear optical crystals: a complete survey* (Springer-Science, 2006).
26. B. N. Carnio and A. Y. Elezzabi, "Investigation of ultra-broadband terahertz generation from sub-wavelength lithium niobate waveguides excited by few-cycle femtosecond laser pulses," Opt. Express **25**(17), 20573–20583 (2017)..
27. A. S. Barker, A. Ballman, and J. Ditzenberger, "Infrared Study of the Lattice Vibrations in $LiTaO_3$," Phys. Rev. B **2**(10), 4233–4239 (1970)..
28. A. S. Barker and R. Loudon, "Dielectric Properties and Optical Phonons in $LiNbO_3$," Phys. Rev. **158**(2), 433–445 (1967).
29. P. L. Kramer, M. K. R. Windeler, K. Mecseki, E. G. Champenois, M. C. Hoffmann, and F. Tavella, "Enabling high repetition rate nonlinear THz science with a kilowatt-class sub-100 fs laser source," Opt. Express **28**(11), 16951–16967 (2020).
30. M. He, M. Xu, Y. Ren, J. Jian, Z. Ruan, Y. Xu, S. Gao, S. Sun, X. Wen, L. Zhou, L. Liu, C. Guo, H. Chen, S. Yu, L. Liu, and X. Cai, "High-performance hybrid silicon and lithium niobate Mach–Zehnder modulators for 100 Gbit s-1 and beyond," Nat. Photonics **13**(5), 359–364 (2019)..
31. M. Zhang, C. Wang, R. Cheng, A. Shams-Ansari, and M. Lončar, "Monolithic ultra-high-Q lithium niobate microring resonator," Optica **4**(12), 1536–1537 (2017).
32. C. Wang, C. Langrock, A. Marandi, M. Jankowski, M. Zhang, B. Desiatov, M. M. Fejer, and M. Lončar, "Ultrahigh-efficiency wavelength conversion in nanophotonic periodically poled lithium niobate waveguides," Optica **5**(11), 1438–1441 (2018).
33. J. Lu, J. B. Surya, X. Liu, A. W. Bruch, Z. Gong, Y. Xu, and H. X. Tang, "Periodically poled thin-film lithium niobate microring resonators with a second-harmonic generation efficiency of 250,000%/W," Optica **6**(12), 1455–1460 (2019)..
34. J. Y. Chen, Z. H. Ma, Y. M. Sua, Z. Li, C. Tang, and Y. P. Huang, "Ultra-efficient frequency conversion in quasi-phase-matched lithium niobate microrings," Optica **6**(9), 1244–1245 (2019)..
35. R. Luo, Y. He, H. Liang, M. Li, and Q. Lin, "Highly tunable efficient second-harmonic generation in a lithium niobate nanophotonic waveguide," Optica **5**(8), 1006–1011 (2018).
36. C. Wang, M. Zhang, X. Chen, M. Bertrand, A. Shams-Ansari, S. Chandrasekhar, P. Winzer, and M. Lončar, "Integrated lithium niobate electro-optic modulators operating at CMOS-compatible voltages," Nature **562**(7725), 101–104 (2018).
37. Y. He, Q. F. Yang, J. Ling, R. Luo, H. Liang, M. Li, B. Shen, H. Wang, K. Vahala, and Q. Lin, "Self-starting bi-chromatic $LiNbO_3$ soliton microcomb," Optica **6**(9), 1138–1144 (2019).
38. C. Wang, M. Zhang, M. Yu, R. Zhu, H. Hu, and M. Loncar, "Monolithic lithium niobate photonic circuits for Kerr frequency comb generation and modulation," Nat. Commun. **10**(1), 978 (2019)..
39. R. Wu, J. Zhang, N. Yao, W. Fang, L. Qiao, Z. Chai, J. Lin, and Y. Cheng, "Lithium niobate micro-disk resonators of quality factors above 10^7," Opt. Lett. **43**(17), 4116–4119 (2018)..
40. E. V. Loewenstein, D. R. Smith, and R. L. Morgan, "Optical Constants of Far Infrared Materials. 2: Crystalline Solids," Appl. Opt. **12**(2), 398–406 (1973).
41. T. J. Parker, J. E. Ford, and W. G. Chambers, "The optical constants of pure fused quartz in the far-infrared," Infrared Phys. **18**(3), 215–219 (1978).
42. N. Ranjkesh, M. Basha, A. Taeb, and S. Safavi-Naeini, "Silicon-on-glass dielectric waveguide—Part II: For THz applications," IEEE Trans. Terahertz Sci. Technol. **5**(2), 280–287 (2015).
43. H. Amarloo, N. Ranjkesh, and S. A. Safavi-Naeini, "Terahertz silicon-BCB-quartz dielectric waveguide: an efficient platform for compact THz systems," IEEE Trans. Terahertz Sci. Technol. **8**(2), 201–208 (2018).
44. R. W. Boyd, *Nonlinear optics* (Academic, 2020).
45. E. Bringuier, A. Bourdon, N. Piccioli, and A. Chevy, "Optical second-harmonic generation in lossy media: Application to GaSe and InSe," Phys. Rev. B **49**(24), 16971–16982 (1994).